

Annual Parallax Measurements of an Infrared Dark Cloud MSXDC G034.43+00.24 with VERA

Tomoharu KURAYAMA,¹ Akiharu NAKAGAWA,¹ Satoko SAWADA-SATOH,² Katsuhisa SATO,² Mareki HONMA,^{2,3}
Kazuyoshi SUNADA,² Tomoya HIROTA,^{2,3} and Hiroshi IMAI¹

¹*Department of Physics and Astronomy, Graduate School of Science and Engineering, Kagoshima University, 1-21-35,
Korimoto, Kagoshima, 890-0065*

²*Mizusawa VLBI Observatory, National Astronomical Observatory of Japan, 2-12, Hoshigaoka-cho, Mizusawa, Oshu, Iwate,
023-0861*

³*Department of Astronomical Sciences, Graduate University for Advanced Studies, 2-21-1, Osawa, Mitaka, Tokyo, 181-8588
kurayama@sci.kagoshima-u.ac.jp*

(Received ; accepted)

Abstract

We have measured the annual parallax of the H₂O maser source associated with an infrared dark cloud MSXDC G034.43+00.24 from the observations with VERA (VLBI Exploration of Radio Astrometry). The parallax is 0.643 ± 0.049 mas, corresponding to the distance of $1.56^{+0.12}_{-0.11}$ kpc. This value is less than the half of the previous kinematic distance of 3.7 kpc. We revise the core mass estimates of MSXDC G034.43+00.24, based on virial masses, LTE masses and dust masses and show that the core masses decrease from the previous estimations of $\sim 1000M_{\odot}$ to hundreds of M_{\odot} . The spectral type derived from the luminosity also changes from O9.5 to B1 in the case of MM1. This spectral type is still consistent with that of the massive star. The radial velocity derived from the flat rotation model is smaller than the observed velocity, which corresponds to the peculiar motion of ~ 40 km s⁻¹ in the line-of-sight direction.

Key words: astrometry — ISM: individual (MSXDC G034.43+00.24) — stars: formation — techniques: interferometric

1. Introduction

Infrared dark clouds (hereafter, IRDCs) are discovered by the observations with ISO (Infrared Space Observatory) and MSX (Midcourse Space Experiment) (P  rault et al. 1996; Carey et al. 1998; Hennebelle et al. 2001), and observed as dark silhouettes against the background radiation of our galaxy in the mid infrared wavelength (P  rault et al. 1996; Egan et al. 1998). They are massive ($\sim 10^2$ – 10^4M_{\odot}), dense ($> 10^5$ cm⁻³), high column density ($\sim 10^{23}$ – 10^{25} cm⁻²), and low temperature (< 25 K) (Egan et al. 1998; Carey et al. 1998; Carey et al. 2000; Tayssier, Hennebelle, P  rault 2002; Simon et al. 2006a; Simon et al. 2006b).

Recently, IRDCs have been known as the sites where massive star formation is active (Rathborne, Jackson, Simon 2006; Rathborne, Simon, Jackson 2007; Pillai et al. 2006; Jackson et al. 2008; Chambers et al. 2009). Various parameters, such as masses and luminosities, have been obtained from many observational studies from the mid-infrared to millimeter wavelengths (e.g., Rathborne et al. 2005; Shepherd et al. 2007; Sanhueza et al. 2010). These parameters depend on distance, and in most cases, kinematic distances have been used to derive the parameters assuming the rotational model of our Galaxy. However, recent annual parallax measurements with VLBI show that kinematic distances tend to be overestimated and sometimes more than the double of those from parallaxes (e.g. Sato et al. 2010a, Motogi et al. 2011). Therefore,

it is important to measure distances toward the sources accurately to know the physical condition of the sources.

Annual parallaxes of galactic sources located at a few kpc from the Sun can be measured from the phase-referencing VLBI observations. Phase-referencing VLBI is technique to observe two adjacent (less than several degrees in the case of 22 GHz-band observations) sources on the sky simultaneously or in the short time interval ($\lesssim 60$ s at 22 GHz band) (Asaki et al. 2007; Thompson, Moran, Swenson 2001). By subtracting the difference of optical path lengths between the target and reference source, it becomes possible to eliminate the short-term fluctuations of the earth’s atmosphere. In addition, the reference position is given by selecting an extragalactic source as the reference source. These benefits enable the astrometry referred to the reference source and, with the long-time integration, the detections of faint sources which is not able to detect with the normal VLBI observations.

Phase-referencing VLBI observations with VERA (VLBI Exploration of Radio Astrometry) and the VLBA (Very Large Baseline Array) derive annual parallaxes of the kilo-parsec scale for the galactic maser sources (e.g., Baba et al. 2009 and references therein; Sato et al. 2010a; Oh et al. 2010; Rygl et al. 2010; Kamohara et al. 2010) after the first successful measurements of annual parallaxes with H₂O masers by Kurayama, Sasao, Kobayashi (2005). It is possible to measure the annual parallaxes when both the maser sources and the adjacent extragalactic reference sources are bright and compact sufficient to observe with

VLBI.

Some IRDCs emit masers such as the H₂O masers and CH₃OH masers (Pillai et al. 2006; Wang et al. 2006; Chambers et al. 2009), so we can measure the annual parallaxes from the phase-referencing VLBI observations of these masers. We used H₂O masers this time because most parallaxes measured with VERA are based on the H₂O maser observations. Wang et al. (2006) surveyed H₂O masers for IRDCs and found that MSXDC G034.43+00.24 has bright H₂O masers. There is also an extragalactic source as a reference source for phase-referencing within 2° from MSXDC G034.43+00.24 (Fomalont et al. 2003). Therefore, this source is one of the most suitable IRDCs to measure the parallaxes with VERA.

MSXDC G034.43+00.24 has a filamentary structure extended over $\sim 9'$ in the declination direction, and four millimeter cores (MM1–MM4) on this filamentary structure (Faúndez et al. 2004; Garay et al. 2004; Rathborne et al. 2005). An IRAS point source (IRAS 18507+0121) and an ultra compact H II region are associated with MM2 (Miralles, Rodrigues, Scalise 1994; Molinari et al. 1998). MM1, MM3 and MM4 have 4.5 μm excesses, which suggest the existence of the ionized or shocked gas. Point sources seen at 24 μm and associated with all four millimeter cores suggest the existence of the warm dust (Rathborne et al. 2005; Chambers et al. 2009). Garay et al. (2004), Rathborne et al. (2005), Rathborne, Jackson, Simon (2006), Shepherd et al. (2007) and Sanhueza et al. (2010) calculated the mass of each millimeter core. VLA observations have detected H₂O masers in MM1, MM3 and MM4 (Wang et al. 2006). No VLBI observation has been conducted for MSXDC G034.43+00.24. The available distances to MSXDC G034.43+00.24 is the kinematic distance only, whose value is 3.7 kpc, from ¹³CO $J=1 \rightarrow 0$ observations (Simon et al. 2006b) and CS(2–1) observations (Bronfman, Nyman, May 1996; Faúndez et al. 2004). Hence, it is very important to measure the annual parallax of this source. Here, we report the results from VERA.

2. Observations

Observations were carried out with VERA four stations. The target maser is the 6₁₆ \rightarrow 5₂₃ transition of H₂O molecules, whose rest frequency is 22.23508 GHz. We monitored at ten epochs from 2006 November to 2008 July with the typical observing duration of 9 hours. The observation dates are listed in table 1. Before this astrometric monitoring, we conducted maser survey observations of four millimeter cores on 2006 October 21.

We conducted phase-referencing VLBI observations of the target source MSXDC G034.43+00.24 and the reference source GPSR5 35.946+0.379 (= VCS2 J1855+0251, hereafter we call this source as the reference source), which is separated by 1.6° from the target source. Using the dual beam system of VERA telescopes (Kawaguchi, Sasao, Manabe 2000; Honma et al. 2008), we observed these two sources simultaneously. For the fringe finding and bandpass calibration, we also observed the calibra-

tor source QSO J1800+3848 ($\alpha_{\text{J2000}} = 18^{\text{h}}00^{\text{m}}24.^{\text{s}}765362$, $\delta_{\text{J2000}} = +38^{\circ}48'30.''69754$) with the both beams every 80 minutes.

Observed signals are filtered with the digital filter bank (Iguchi et al. 2005) and outputted in the form of sixteen IFs. Each IF contains 16-MHz bandwidth signal. One IF contains the signal of the target (maser) source. The other fifteen IFs contain the signals of the reference (continuum) source. The recording rate is 1024 Mbps (32 Msps \times 2 bit sample⁻¹ \times 16 IF). The correlation is performed with Mitaka FX correlator. The correlator integrates the output data for 1 s in the time domain. In the frequency domain, the output data are 8 MHz bandwidth with the 512 frequency points for one maser IF and 16 MHz bandwidth with the 64 frequency points for fourteen continuum IFs. One continuum IF is abandoned in the data reduction process. The velocity resolution at the correlator output is 0.21 km s⁻¹ for the maser IF and 3.4 km s⁻¹ for the continuum IFs.

The measurements of the annual parallax of MSXDC G034.43+00.24 require a special care because this source has a low-declination of $\sim +1^{\circ}$. This causes a decrease of the positional accuracy in the declination direction. In VLBI observations, we vary the measurement points on the uv plane, which corresponds to the aperture of the normal single-dish telescopes, by changing the positional relationship between the stations and the sources using the earth's spin. The loci of measured points on the uv plane draw parts of the ellipses for high-declination sources, but they draw almost straight lines in the right-ascension direction for low-declination sources. Thus the positional accuracy in the declination direction decreases especially in the case of the small number of stations, that is, small numbers of baselines and observing points in the declination direction. In our parallax measurement, we used only the right-ascension components in order to avoid this effect. The reason of large uncertainty in the declination direction is also described in §4.3.1.

3. Data Reduction

Data reduction was done with NRAO (National Radio Astronomy Observatory) AIPS (Astronomical Image Processing System) software and DIFMAP. The functions neither AIPS nor DIFMAP provide were added with external programs. The steps of our data reduction are as follows :

1. Amplitude calibration for all sources
2. Bandpass calibration for all sources using calibrator source
3. Modification of tracking model in Mitaka FX correlator
4. Time and frequency integration
5. Calibration of clock parameters (Global fringe search for calibrator source)
6. Global fringe search for reference source
7. Imaging of reference source with self-calibration
8. Phase referencing (Subtracting the phases of reference source from those of target source)

Table 1. Observation summary.

epoch	date	day offset*	synthesized beam†
1st	2006 Nov 16	-297	1.29×0.86 mas at -53°
2nd	2007 Jan 04	-248	1.40×0.79 mas at -50°
3rd	2007 Feb 10	-211	1.39×0.82 mas at -52°
4th	2007 Mar 25	-168	1.36×0.81 mas at -52°
5th	2007 May 04	-128	1.28×0.74 mas at -53°
6th	2007 Aug 06	-34	1.32×0.81 mas at -44°
7th	2007 Oct 02	23	1.33×0.80 mas at -45°
8th	2008 Jan 04	117	1.43×0.79 mas at -49°
9th	2008 Apr 12	216	1.35×0.82 mas at -48°
10th	2008 Jul 02	297	1.27×0.81 mas at -39°

* Offset from the center date (2007 September 9) of the term.

† The lengths of major and minor axes and the position angle of the major axis.

9. Dual-beam calibration with ‘horn-on-dish’ method (Honma et al. 2008)
10. Calibration of Doppler effect
11. Imaging of target source with CLEAN
12. Measuring the position and flux by fitting elliptical Gaussians

The details of the data reduction procedure for an observing epoch are shown in Appendix 1.

‘Modification of tracking model in Mitaka FX correlator’ (step 3) is needed because the tracking model in Mitaka FX correlator does not have sufficient accuracy for astrometric measurements. We changed it to the newly calculated model with CALC3/MSOLV (Jike et al. 2005; Manabe, Yokoyama, Sakai 1991). In this recalculation, we used the equatorial coordinates for the target source MSXDC G034.43+00.24 as $\alpha_{J2000} = 18^{\text{h}}53^{\text{m}}19^{\text{s}}00000$, $\delta_{J2000} = +1^{\circ}24'08''0000$ and for the reference source GPSR5 35.946+0.379 = VCS2 J1855+0251 as $\alpha_{J2000} = 18^{\text{h}}55^{\text{m}}35^{\text{s}}43649$, $\delta_{J2000} = +2^{\circ}51'19''5623$ (Fomalont et al. 2003). The equatorial coordinate for the target source corresponds to that of the millimeter core MM1 (Rathborne et al. 2005). The new recalculated model contains the estimation of the wet component of the earth’s atmosphere from GPS data at VERA stations (Honma, Tamura, Reid 2008).

Before ‘imaging of target source with CLEAN’ (step 11), we need to know the position where we make images. Only the H₂O masers associated with the millimeter core MM1 was imaged (see §4.1). Producing the fringe-rate map with our own program from the results of the global fringe search for the flux-peak frequency channel, we find a maser cluster as shown in figure 1. We made the images for the eight features in the maser cluster at which we found the masers for the data on 2008 January 4. We adopted maser features only when their radiation is confirmed over three or more frequency channels.

In ‘measuring the position and flux by fitting elliptical Gaussians’ (step 12), we fit the elliptical Gaussians for the five regions where we detected maser emission during more than two continuous epochs (see, table 2). We adopted the peak positions as the positions of maser features. In this paper, maser features denotes maser emissions detected

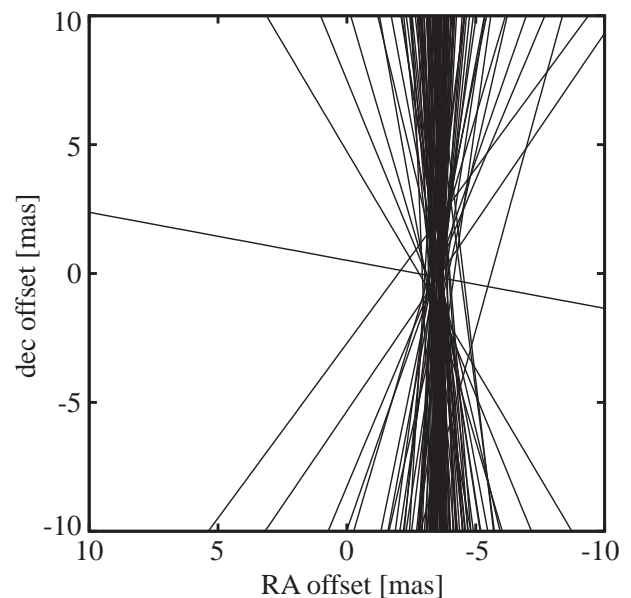


Fig. 1. Fringe rate map of the H₂O masers at the millimeter core MM1 made from the results of the global fringe search with AIPS. The map origin is located at the position of the target source modified in the recalculation of the tracking model whose equatorial coordinate is $\alpha_{J2000} = 18^{\text{h}}53^{\text{m}}19^{\text{s}}00000$, $\delta_{J2000} = +1^{\circ}24'08''0000$. Each line shows the possible position of the masers calculated from one rate value. Maser clusters are placed at the crossing point of lines. This map is obtained from the data on of 2008 January 4 at the radial velocity of $v_{\text{LSR}} = 56.5 \text{ km s}^{-1}$.

at multiple frequency points at the same position on the sky. Positions are measured at the frequency channels at which the flux is largest among the detected frequency channels. Detected maser features are compact sufficient for the position measurements, shown in Figure 2. When multiple maser features are detected in an image at an epoch, we used the feature which has closest declination value to the other epochs. Figure 3 shows an example of the selection of maser features in this process. From this figure, we can find that declinations are better for this selection than right ascensions although declinations have large position errors shown in §4.3.1.

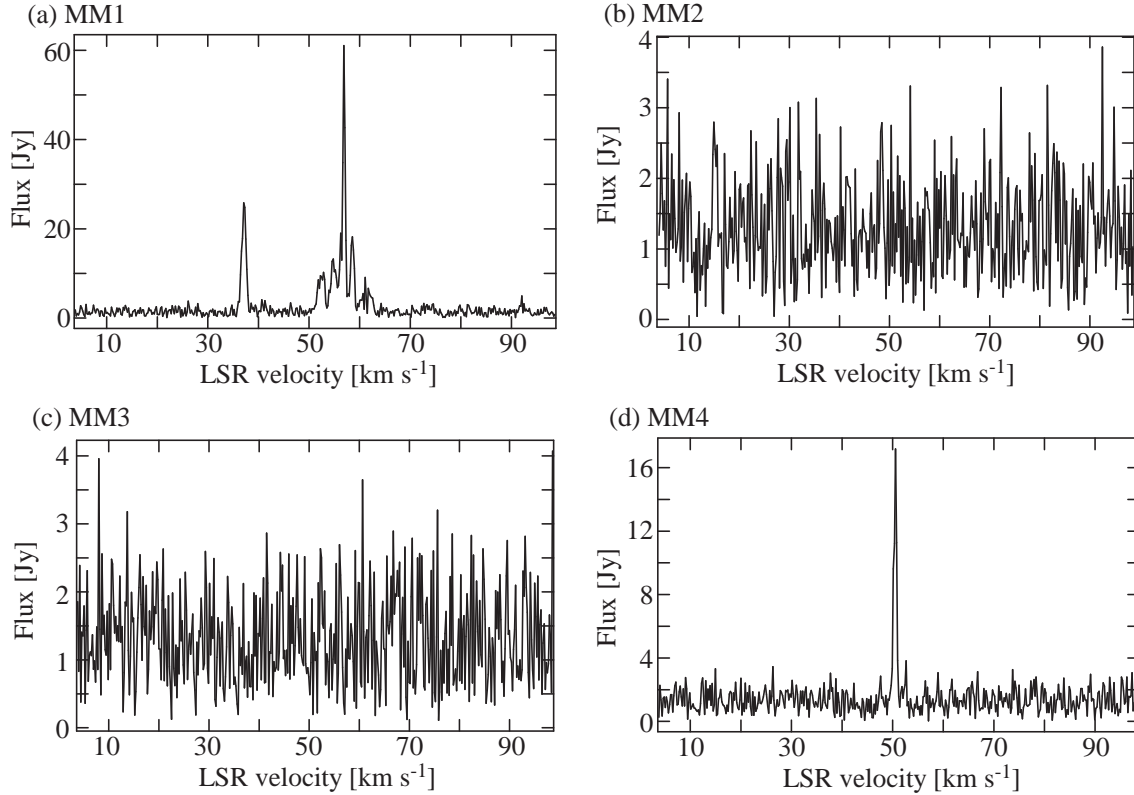


Fig. 4. Cross-power spectra of the H₂O masers at the millimeter-core positions: (a) MM1, (b) MM2, (c) MM3, and (d) MM4. They are obtained from the data on 2006 October 21 at Mizusawa–Iriki baseline. The integration time of data is 5 minutes. We integrated the data after the phase-referencing, which gets rid of the short-time fluctuation of the earth’s atmosphere and enables the long-term integration.

4. Results

4.1. Survey Results of Masers

Figure 4 shows the cross-power spectra obtained from the survey observations on 2006 October 21 at the four millimeter-core positions. We find that the H₂O masers are detected in MM1 and MM4, but are not detected in MM2 and MM3. Comparing with the VLA observations in 2006 (Wang et al. 2006), the detection is not consistent only for MM3. This may be caused by the time variation of masers or the extended emission of the source structure, that is, masers in MM3 could be resolved out with the long (~ 2000 km) baselines of VERA.

From this result, we observed the millimeter-core MM1 for the annual parallax measurements from the observation on 2006 November 16.

4.2. Derivation of Parallax with Least Square Fitting

Figure 5 and 6 show the movements of maser features measured with respect to the reference source. The movements look like the combination of the parallax motion and the linear motion in the right-ascension direction, but have large scatter over 20 mas in the declination direction. This is because the declination of the target source ($\sim +1^\circ$) is small. As shown in figure 7, there are large sidelobes of the synthesized beam in the declination direction. The stable and uncalibrated component of the

earth’s atmosphere affect the positions in the declination direction. The details of this effect is discussed in §4.3.1. We used only the data of the right-ascension direction this time.

We carried out the least square fitting only with the right-ascension data to derive the annual parallax. The model is the combination of the movement by the annual parallax and the linear motion. The movement except by the annual parallax, such as the galactic rotation, the peculiar motion of the Sun, are contained in the linear motion. This is expressed as the following equation:

$$\alpha^{(i)}(t) \cos \delta = \varpi (-\sin \alpha \cos \odot + \cos \varepsilon \cos \alpha \sin \odot) + (\mu_\alpha^{(i)} \cos \delta) t + \alpha_0^{(i)} \cos \delta, \quad (1)$$

where $\alpha^{(i)}(t)$ is the observed right ascension of the i ’th maser feature at the time t , α and δ are the right ascension and declination of the target source respectively, ϖ is the annual parallax, \odot is the ecliptic longitude of the Sun and ε is the obliquity of ecliptic. $\mu_\alpha^{(i)} \cos \delta$ is the right-ascension component of the linear motion of the i ’th maser feature, t is the day offset from the center of the observation term used for the parallax measurements, shown in table 1 and $\alpha_0^{(i)}$ is the right ascension of i ’th maser feature at the time $t = 0$ (Green 1985).

Table 2 summarizes the detection of masers at each feature and at each epoch. Maser features detected during

Table 2. Detection at each feature and epoch.

Feature Number	v_{LSR} [km s $^{-1}$]	RA* [arcsec]	dec* [arcsec]	Integrated flux at each epoch [Jy] †									
				1st	2nd	3rd	4th	5th	6th	7th	8th	9th	10th
1	88.7	-3.632	+0.088	...	(1.4)	(1.1)	(2.6)	(3.6)
2	61.7	-3.489	+0.819	(3.4)	5.9	8.8	3.8	(5.7)	3.1	2.5	9.4	(2.8)	...
3	59.4	(-3.367)	(-0.036)	...	(2.1)	(5.2)	...	(2.2)	...
4	57.9	-3.425	-0.061	(2.4)	(4.4)	(3.9)	(0.8)	(2.0)
5	57.3	-3.303	-0.035	(1.7)	(3.0)	1.0	(5.3)	22.4	11.5
6	56.5	-3.672	+0.107	(3.2)	(6.6)	(5.8)	(4.5)	(2.6)	(27.3)	(54.5)	...
7	53.9	-3.425	+0.657	2.2	(8.7)	3.8	8.7	19.2	(5.8)	...
8	43.4	-3.392	-0.048	(5.1)	(0.5)	...

* Offset values from the right ascension and declination used in the modification of the tracking model : $\alpha_{\text{J2000}} = 18^{\text{h}}53^{\text{m}}19^{\text{s}}0$, $\delta_{\text{J2000}} = +1^{\circ}24'08''$. Values without parentheses are the offsets at 8th epoch on 2008 January 4. Values with parentheses are the averages of the detected epochs.

† Numbers without parentheses denote that the data of the features and epochs are used for the annual parallax measurements. Numbers with parentheses denote that the data are not used.

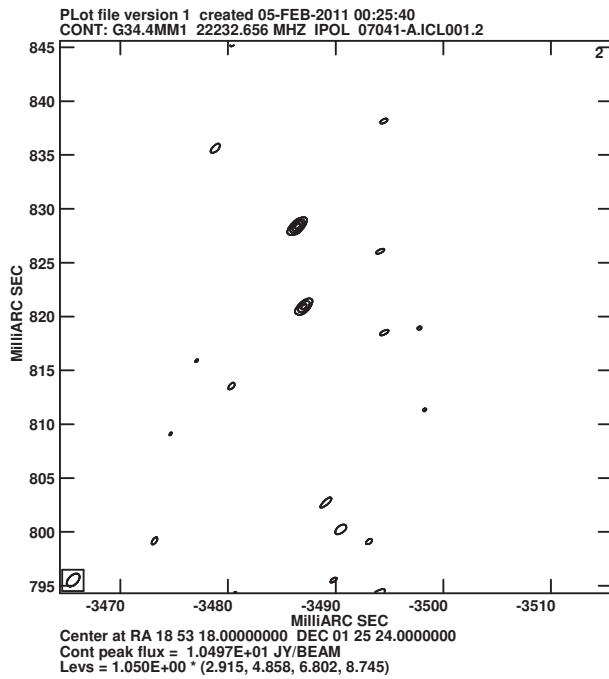


Fig. 2. An example of the phase-referenced images of detected maser features. The phase-referenced image of maser feature No. 2 at 3rd epoch on 2007 February 10. Contours are 3σ , 5σ , 7σ and 9σ brightness level, where σ is the rms noise level of $0.99 \text{ Jy beam}^{-1}$. Maser features are compact sufficient to measure their positions.

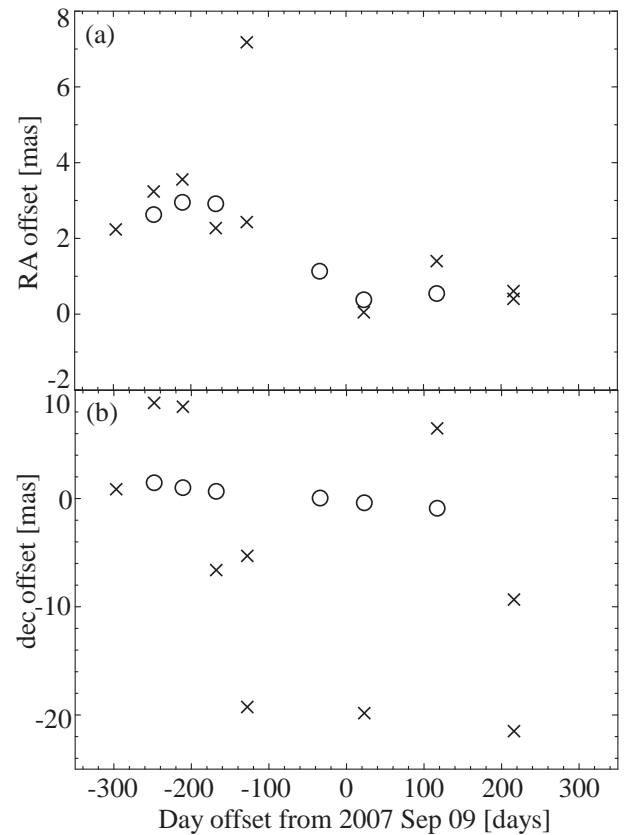


Fig. 3. Maser-feature selection for the feature No. 2 when multiple maser features are detected in an image at an epoch. (a) Plot of right ascensions versus time. (b) Plot of declinations versus time. In both panels, open circles (O) show the maser features which are used for the parallax fitting, and crosses (x) show the maser features which are not used for the parallax fitting. From (a), it is difficult to know which feature should be used, but we can easily select from (b) although declination data have large position errors shown in §4.3.1.

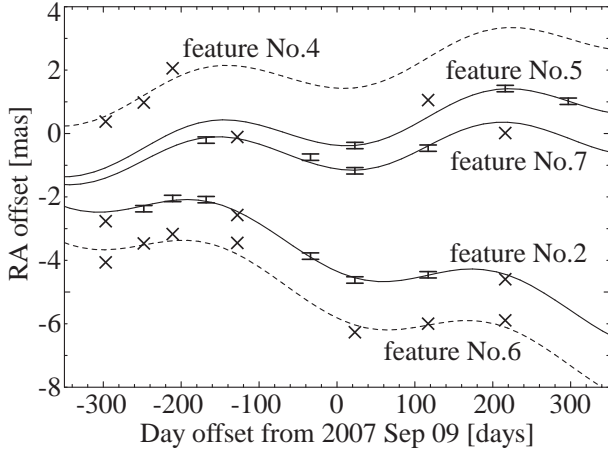


Fig. 5. Observed data points in the right ascension direction and the least square fitting for the annual parallax measurements. Table 1 shows the correspondence between the values of day offsets from 2007 September 9 (horizontal axis) and the observation dates. The offset in the vertical axis for each feature is included just for the display. The observed points are the center of the error bars. Crosses (\times) show the data points which are not used for the parallax fitting. The amplitudes of uncertainty are 0.101 mas, which is calculated from the assumption of $(\text{reduced } \chi^2) = \chi^2/\nu = 1$. Feature numbers are same as those in table 2. Solid curves are the results of the least-square fitting as shown in table 3. Dashed curves show the movements of features which are derived from the least square fitting for calculating linear motions and initial positions only, assuming the parallax of $\varpi = 0.643$ mas derived from the fitting.

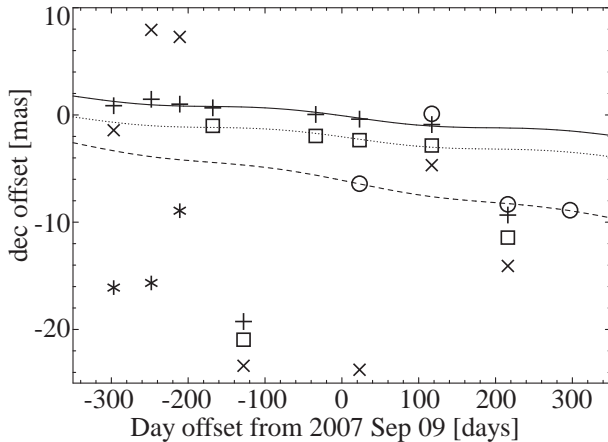


Fig. 6. Plot of the observed data points in the declination direction against time. Table 1 shows the correspondence between the day offsets from 2007 September 9 (horizontal axis) and the observation dates. The offset in the vertical axis is included for each feature for the display. Crosses (+) show the positions of feature number 2, asterisks (*) of feature number 4, circles (○) of feature number 5, Crosses (\times) of feature number 6 and squares (□) of feature number 7. Feature numbers are same those in table 2. Solid, dotted and dashed curves show the movements of feature number 2, 7 and 5 respectively, which are derived from the least square fitting for calculating linear motions and initial positions only, assuming the parallax derived from right-ascension data $\varpi = 0.643$ mas.

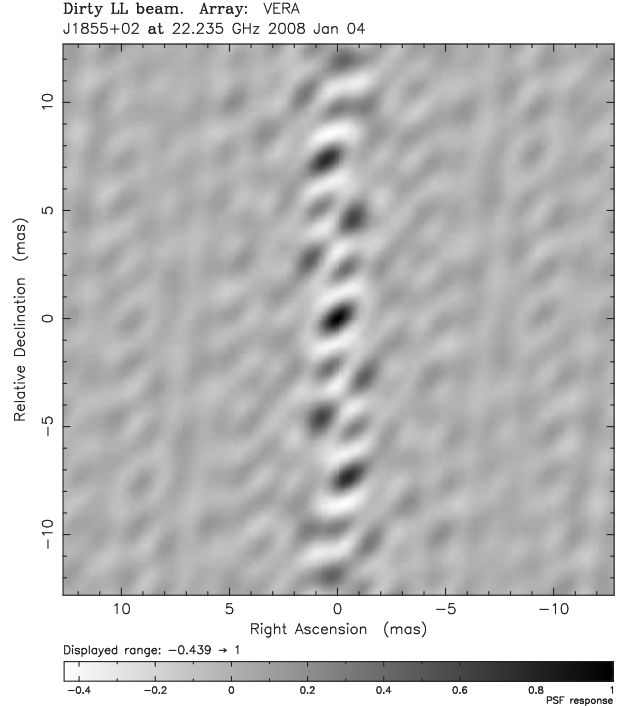


Fig. 7. The synthesized beam of VERA four stations in the observation on 2008 January 4. Strong sidelobes are found in the declination direction.

Table 3. Results of the fitting of the annual parallax and the linear motions

	ϖ^* 0.643 \pm 0.049 mas	
Feature [†] Number	$\mu_{\alpha}^{(i)} \cos \delta^{\ddagger}$ [mas yr ⁻¹]	$\alpha_0^{(i)} \cos \delta^{\S}$ [mas]
2	-2.19 \pm 0.12	-3488.77 \pm 0.05
5	0.98 \pm 0.21	-3303.80 \pm 0.12
7	0.46 \pm 0.19	-3425.55 \pm 0.05

* Value of the annual parallax.

† Corresponding to the feature numbers in table 2.

‡ Right-ascension components of the linear motions.

§ Offsets in the right-ascension direction at $t = 0$ on 2007 September 9 from the position used in the modification of tracking model $\alpha_{J2000} = 18^{\text{h}}53^{\text{m}}19^{\text{s}}.0$, $\delta_{J2000} = +1^{\circ}24'08''$.

more than two continuous epochs are used for the parallax measurements. The data points which are not on the declination trend are omitted from the fitting. This is because we can not solve parameters when we can not use data of more than two epochs. When we include one new maser feature, we need two extra fitting parameters: the initial position and the linear motion. We fitted for three maser features, so seven parameters are fitted : one common ϖ , five $\mu_{\alpha}^{(i)}$, five $\alpha_0^{(i)} \cos \delta$. The total number of data points is twenty-nine, as shown in table 2.

Figure 5 and table 3 show the results of fitting. The derived annual parallax is 0.643 ± 0.049 mas, corresponding to the distance of $1.56^{+0.12}_{-0.11}$ kpc. This distance is smaller than the half of the previous kinematic distance of 3.7 kpc.

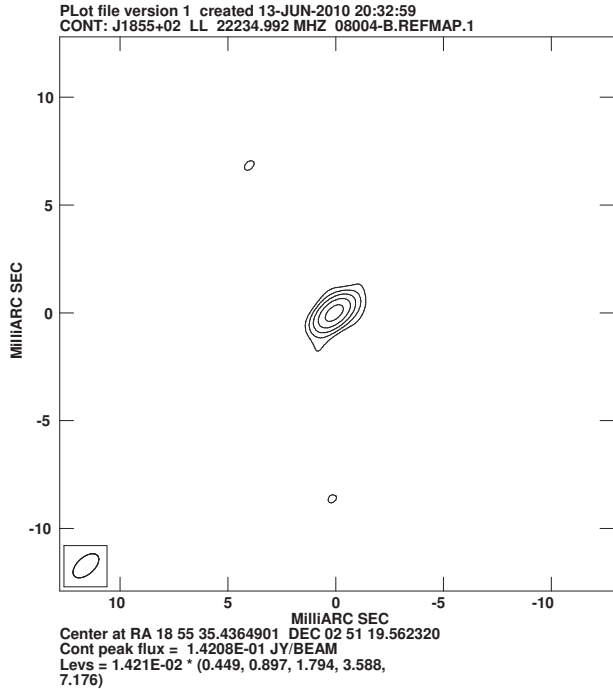


Fig. 8. Imaging result of the reference source GPSR5 35.946+0.379 = VCS2 J1855+0251 with VERA four stations at 22 GHz band. The observation date is 2008 January 4. Contours are 3σ , 6σ , 12σ , 24σ and 48σ brightness level, where σ is the rms noise level of $2.1 \text{ mJy beam}^{-1}$.

4.3. Uncertainty of Each Epoch

Uncertainty at one epoch is calculated by assuming that the uncertainty values of all epochs are same and that (reduced χ^2) = $\chi^2/\nu = 1$, where χ^2 is the squared sum of the residuals of fitting over the square of the uncertainty of one epoch, ν is the degree of freedom in the fitting, the total number of data points minus the total number of parameters. In our fitting, $\nu = 29 - 11 = 18$. The uncertainty at one epoch is 0.101 mas . The uncertainty of fitted parameters is calculated from this value with the normal least square fitting method. Most of the uncertainty is the stable component of the earth's atmosphere of about 0.2 mas , as discussed in §4.3.1.

The uncertainty from the structure of the reference source is small. Figure 8 shows the imaging result of the reference source. This source structure has little change over the all observation epochs used for the parallax measurements. We used same stations in all observing epochs, so the measurement points on the uv plane are basically same.

In order to evaluate the uncertainty of the parallax measurements from the structure of the reference source, we calculated the worst value of the uncertainty as follows. The delay time, optical path length divided by the speed of light, caused by the source structure $\tau(u, v, \omega)$ is given by

$$\tau(u, v, \omega) = \frac{d}{d\omega} \left\{ \arg \left[\iint B(x, y) e^{-2\pi i(ux+vy)} dx dy \right] \right\}, (2)$$

where $B(x, y)$ is the brightness distribution of the reference source, x and y are the coordinates of the right-ascension and declination direction respectively, $\omega = 2\pi\nu$ and ν is the observing frequency (Fujishita 1983; Charlot 1990). For the simple calculations, we set $B(x, y)$ as the sum of the point sources obtained from CLEAN, $B(x, y) = \sum_i B_{0i} \delta(x_i, y_i)$, and approximate $d/d\omega \sim 1/\omega = 1/(2\pi\nu)$ and $2\pi\nu\tau(u, v, \omega) \sim 2\pi\sqrt{u^2+v^2}\Delta x$, where Δx is the positional error. Then, so we approximate $2\pi\nu\tau(u, v, \omega) \sim 2\pi\sqrt{u^2+v^2}\Delta x$ where Δx is the positional error. Then

$$\Delta x \sim \frac{1}{2\pi\sqrt{u^2+v^2}} \arg \left(\sum_i B_{0i} e^{-2\pi i(ux_i+vy_i)} \right). (3)$$

We calculated this value for the data on 2008 January 4 and the maximum values of u and v of $u_{\max} = 1.4 \times 10^8$ and $v_{\max} = 1.2 \times 10^8$ in the unit of the wavelength. The result is $\Delta x = 0.045 \text{ mas}$. The uncertainty from the structure of the reference source has a small fraction in the each epoch's uncertainty of 0.101 mas .

4.3.1. Uncertainty from Stable Component of the Earth's Atmosphere

In the phase-referencing VLBI observations, the effect of the earth's atmosphere is removed by taking the differences of the optical path lengths between the target and reference sources. With this process, we can remove the short-term fluctuations of the earth's atmosphere, which is the largest atmospheric effect in VLBI observations. However, the elevation angle of the target and reference sources are not completely same, so it is impossible to remove the effect of airmass, that is, the stable component of the earth's atmosphere (Honma, Tamura, Reid 2008). Assuming the plane-parallel approximation of the earth's atmosphere, the effect of airmass is given by in the unit of the optical path length

$$l_{ij} = L_j \sec z_{ij}, (4)$$

when source i is observed with the station j , where L_j is the airmass effect in the zenith direction in the unit of the optical path length, and z_{ij} is the zenith angle of the observed source. In phase-referencing observations, we subtract the optical path lengths between the target and reference sources. After the phase-referencing, the following airmass effect remains:

$$l_{1j} - l_{2j} = L_j (\sec z_{1j} - \sec z_{2j}). (5)$$

We evaluated quantitatively how much this effect contributed to the uncertainty of our astrometric observations in the following way: (1) Giving the optical-path-length offset in the zenith direction by the earth's atmosphere, L . We added this offset to Ishigakijima station only for the simplicity because this station is most humid and hence, L could have large uncertainty. We changed L at 1 cm step in the range of $-30 \text{ cm} \leq L \leq 30 \text{ cm}$. (2) Adding the phase correction of

$$\frac{2\pi}{\lambda} L [\sec z_t(t) - \sec z_r(t)] (6)$$

obtained from the plane-parallel approximation to all visibilities of the target source at the baselines including Ishigakijima station, where λ is the observation wavelength, $z_t(t)$ and $z_r(t)$ are the zenith angle of the target and reference source at the time t , respectively. We used the relationship between the phase ϕ and the optical path length l of $\phi = (2\pi/\lambda)l$. (3) Imaging the target source from the phase-corrected visibilities without CLEAN, and deriving the flux and position of the maser feature by picking up the pixel of the flux peak.

Figure 9 shows the result of above evaluation for the maser feature in the feature number 5 and for the observation on 2008 January 4. As discussed by Honma, Tamura, Reid (2008), the true atmospheric path length should maximize the peak brightness. There are not so large offset in the right-ascension and declination direction at the atmospheric path length of about -8 cm, but the offset becomes large, more than 10 mas in the declination direction at the atmospheric path length of around -22 cm. Such a large L would not be expected if GPS calibration is included (Honma, Tamura, Reid 2008) in which case it is normally a few centimeters. Therefore, the stable component of the earth's atmosphere might be one of the largest causes of the large position offsets in the declination direction seen in figure 5, but we can not deny other causes, for example the structure effect of the target maser source, large offsets ($\sim 4''$) from the right ascension of the tracking model. This atmospheric effect is the most part of the uncertainty in right ascension direction at each epoch of 0.101 mas, because the offset value in the right-ascension direction in the range of $-25 \text{ cm} < L < 0 \text{ cm}$ is about ± 0.1 mas.

4.4. Other Approaches for Poor Declination Measurements

From figure 9, we can find that right ascensions are also affected by the stable component of the earth's atmosphere. In order to evaluate this, we carried out the fitting of the annual parallax with the following six methods:

1. Using five features (feature numbers 2, 4, 5, 6 and 7). Using all epochs, also including the data points which are far from the declination trends (1st, 5th and 9th epochs for feature number 2; 8th epoch for feature number 5; 5th and 9th epochs for feature number 7) except the 1st and 2nd epochs of feature number 5 which have a long time gap against the later epochs. Using the data of right ascension only.
2. Using three features which have trends in the declination measurements (feature numbers 2, 5 and 7). Using all epochs, also including the data points which are far from the declination trends (1st, 5th and 9th epochs for feature number 2; 8th epoch for feature number 5; 5th and 9th epochs for feature number 7) except the 1st and 2nd epochs of feature number 5 which have a long time gap against the later epochs. Using the data of right ascension only.

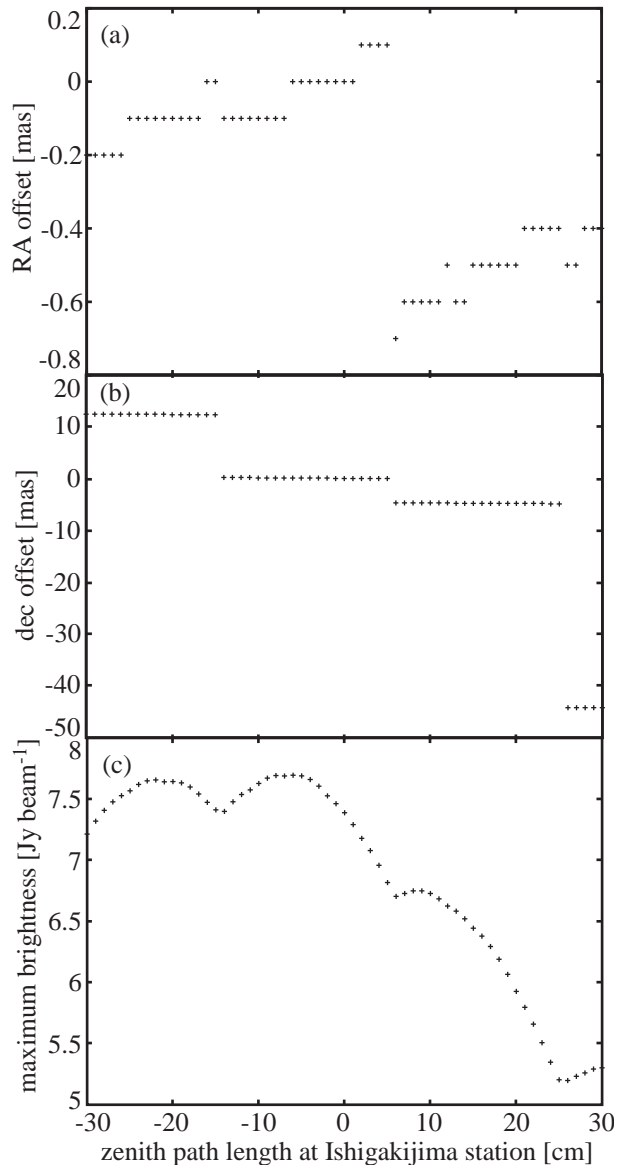


Fig. 9. (a) Right-ascension offset, (b) declination offset, (c) brightness of the peak-flux pixel against the optical path length of the zenith direction by the earth's atmosphere. In (a) and (b), the right ascension and declination not added the atmospheric effect are set to zero. We evaluated for the maser feature in the feature number 5 observed on 2008 January 4. Since the pixel size is 0.1 mas and since the resolution of right-ascension and declination is the pixel size, the quantized variation in (a) is caused by the pixel size. The nature of quantized variation in (b) may be the effect of the sidelobe pattern (see figure 7).

3. Using three features which have trends in the declination measurements (feature numbers 2, 5 and 7). Excluding the epochs at which the declination data are far from the trends (1st, 5th and 9th epochs for feature number 2; 8th epoch for feature number 5; 5th and 9th epochs for feature number 7) and the 1st and 2nd epochs of feature number 5 which have a long time gap against the later epochs. Using the data of right ascension only. This is the method we adopt at §4.2.
4. Same as the method No. 3, but using the data of both right ascension and declination.
5. Using three features which have trends in the declination measurements (feature numbers 2, 5 and 7). Using all epochs, also including the data points which are far from the declination trends (1st, 5th and 9th epochs for feature number 2; 8th epoch for feature number 5; 5th and 9th epochs for feature number 7) except the 1st and 2nd epochs of feature number 5 which have a long time gap against the later epochs. For the epochs at which the declination data are far from the trends, we tried to recover the declination by setting the CLEAN boxes at the likely sidelobes from the trends of declination data. In two epochs, 5th and 9th epochs for feature number 7, we failed this recovery, so we omitted them from the fitting. Using the data of right ascension only.
6. Same as the method No. 5, but using the data of both right ascension and declination.

Table 4 summarizes the result of these fitting. Basically, all fitting results of annual parallax coincide in the error range. Because the method No. 3 has smaller error than the methods No. 1, 2 and 5, right-ascension data also have large errors when their declination data have large errors. Comparing the errors of methods No. 3 and 5, we find that we can not recover these large-declination-error data by setting the CLEAN boxes at the likely sidelobes from the trends on declination data. Comparing method No. 3 and 4, or method No. 5 and 6 show that the declination data have larger errors than the right ascension data even when we try to recover declinations with the settings of CLEAN boxes. In our observations, it might be better not to use the declination data for the fitting of annual parallax. We adopted the fitting method No. 3 because it is the best fit and does not include bad data.

5. Discussion

5.1. Modification of Physical Parameters of Star Forming Regions

The distance to the target source MSXDC G034.43+00.24 becomes less than half of the kinematic distance of 3.7 kpc. This changes the parameters of the star forming regions in this infrared dark cloud. We discuss some examples of them.

Sanhueza et al. (2010) estimates the virial mass of each core from the following equation, assuming the spherical

shape of each core and ignoring the magnetic field and external forces:

$$\frac{M_{\text{vir}}}{M_{\odot}} = B \left(\frac{R}{\text{pc}} \right) \left(\frac{\Delta v}{\text{km s}^{-1}} \right)^2, \quad (7)$$

where Δv is the mean line width, R is the radius of the cloud, B is the constant depending on the density profile of the cloud. They calculated with $B = 210$, corresponding to the uniform density. Virial mass M_{vir} is proportional to the distance, because M_{vir} is proportional to the radius.

They also calculated the LTE (local thermodynamic equilibrium) masses from the observations of the $^{13}\text{CO}(3 \rightarrow 2)$ and $\text{C}^{18}\text{O}(3 \rightarrow 2)$ lines. Assuming that $\text{C}^{18}\text{O}(3 \rightarrow 2)$ is emitted under the LTE condition and this emission is optically thin, LTE mass M_{LTE} is calculated from the following formula:

$$\frac{M_{\text{LTE}}}{M_{\odot}} = 0.565 \left(\frac{\mu_m}{2.72 m_{\text{H}}} \right) \left(\frac{[\text{H}_2/\text{C}^{18}\text{O}]}{3.8 \times 10^6} \right) \left(\frac{D}{\text{kpc}} \right)^2 \frac{(T_{\text{ex}} + 0.88) \exp(15.81/T_{\text{ex}})}{1 - \exp(-15.81/T_{\text{ex}})} \iint \tau_{18} dv d\Omega, \quad (8)$$

where μ_m is the mean molecular weight per H_2 molecule, m_{H} is the mass of the hydrogen atom, $[\text{H}_2/\text{C}^{18}\text{O}]$ is the abundance ratio of C^{18}O relative to H_2 , D is the distance, T_{ex} is the excitation temperature, which is employed to be $T_{\text{ex}} = 30$ K, τ_{18} is the optical depth of the $\text{C}^{18}\text{O}(3 \rightarrow 2)$ line, v is the radial velocity in the unit of km s^{-1} , Ω is the solid angle in the unit of arcmin^2 . They derived τ_{18} from the ratio of the observed brightness temperatures of $\text{C}^{18}\text{O}(3 \rightarrow 2)$ to $^{13}\text{CO}(3 \rightarrow 2)$, assuming $[^{13}\text{CO}/\text{C}^{18}\text{O}] = 7.6$. LTE mass is proportional to the square of the distance.

Rathborne, Jackson, Simon (2006) estimated the dust mass from the 1.2 mm continuum observations with the following equation:

$$M_{\text{dust}} = \frac{F_{\nu} D^2}{\kappa_{\nu} B_{\nu}(T_{\text{dust}})}, \quad (9)$$

where M_{dust} is dust mass, F_{ν} is the observed flux density, D is the distance, κ_{ν} is the dust opacity per unit mass, $B_{\nu}(T_{\text{dust}})$ is the Planck function at the dust temperature T_{dust} . They adopted $\kappa_{1.2\text{mm}} = 1.0 \text{ cm}^2 \text{g}^{-1}$, gas to dust mass ratio of 100, and the dust temperature of $T_{\text{dust}} = 15$ K. Dust mass is also proportional to the square of the distance.

Table 5 shows the masses calculated from the previous distance $D = 3.7$ kpc and our distance $D = 1.56$ kpc. The resultant masses become one order small, and the most massive core is no more than thousand M_{\odot} .

Rathborne et al. (2005) derived the bolometric luminosities from the standard graybody fitting of the spectral energy distribution (SED) between the mid infrared and millimeter wave. They assumed that the cores are isothermal and that their radii are $15''$. The parameters derived from the fitting are the emissivity index β , the optical depth at $250 \mu\text{m}$ $\tau_{250\mu\text{m}}$, the dust temperature T_{dust} , and the bolometric luminosity L_{bol} . Furthermore, the luminosity is constant for the high-mass protostar during the evolution from the protostar to the main-sequence, so the

Table 4. Result of various fittings for the annual parallax

No.	Method	RA/dec	ϖ^*	σ^\dagger	N^\ddagger	n^\S	ν^\parallel
			[mas]	[mas]			
1	five features, all epochs	RA only	0.714 ± 0.060	0.212	29	11	18
2	three features, all epochs	RA only	0.624 ± 0.060	0.182	19	7	12
3	three features, epochs on dec trend	RA only	0.643 ± 0.049	0.101	13	7	6
4	three features, epochs on dec trend	RA and dec	0.553 ± 0.083	0.181	26	13	13
5	three features, all epochs, forced CLEAN boxes	RA only	0.726 ± 0.066	0.177	17	7	10
6	three features, all epochs, forced CLEAN boxes	RA and dec	0.625 ± 0.095	0.269	34	13	21

* Annual parallax

† Uncertainty in one epoch

‡ Total number of data points

§ Total number of calculated parameters

|| Degree of freedom in the fitting

Table 5. Physical parameters of the star forming region MSXDC G034.43+00.24

Millimeter Core	Values at the Kinematic Distance of $D = 3.7$ kpc				Values at Our Distance of $D = 1.56$ kpc				Reference
	MM1	MM2	MM3	MM4	MM1	MM2	MM3	MM4	
Virial Mass	1130	1510	1370	...	476	637	578	...	(1)
LTE Mass	330	1460	59	260	(1)
Dust Mass	1187	1284	301	253	211	228	54	45	(2)
L_{bol}	32000	...	9000	12000	5700	...	1600	2100	(3)
Spectral Type	O9.5	...	B0.5	B0.5	B1	...	B3	B2	(3)

The unit of masses and luminosities are M_\odot and L_\odot , respectively.

Reference : (1) Sanhueza et al. (2010), (2) Rathborne, Jackson, Simon (2006), (3) Rathborne et al. (2005)

bolometric luminosities tell us the corresponding spectral types of protostars. These values are also shown in table 5. They are still early B type star with the mass $\sim 10M_\odot$.

5.2. The Position and Motion on the Galactic Plane

MSXDC G034.43+00.24 is located at the closer part of Sagittarius-Carina arm. Figure 10 shows the position of MSXDC G034.43+00.24 at the distance of 1.4 kpc derived from our annual parallax. The background is cited from Sato et al. (2010a). The black lines and points are the model of the Galaxy by Georgelin, Georgelin (1976) and the gray by Taylor, Cordes (1993), which is modified for the better fit of the kinematic distances by Downes et al. (1980). Taylor, Cordes (1993) introduced a ‘‘bump’’ structure in Sagittarius arm, but our parallax measurement does not support it. As Sato et al. (2010a) proposed, the ‘‘bump’’ may be caused by the errors of kinematic distances.

It might be possible that MSXDC G034.43+00.24 has a large peculiar motion in our Galaxy. When we assume the flat rotation model, the Galactic rotation $V_0 = 220 \text{ km s}^{-1}$ and the distance to the Galactic center $R_0 = 8.5 \text{ kpc}$, the radial velocity of this source is calculated to be $v_{\text{LSR}} = 19 \text{ km s}^{-1}$. The observed radial velocity of the C^{18}O line is about 58 km s^{-1} (Rathborne et al. 2005), which is less than the calculated velocity by about 40 km s^{-1} . This might be the line-of-sight component of the peculiar motion. Furthermore, comparing with other

star-forming regions at almost the same galactic latitude such as G35.20–0.74 and G35.20–1.74, whose distances are measured from parallaxes by Zhang et al. (2009) of $2.19^{+0.24}_{-0.20} \text{ kpc}$ and $3.27^{+0.56}_{-0.42} \text{ kpc}$, respectively, MSXDC G034.43+00.24 is closer to the Sun. More annual parallax measurements of Sagittarius-Carina-arm sources with VERA reveal the structure of Sagittarius-Carina arm.

6. Summary

We carried out the phase-referencing VLBI observations of an infrared dark cloud MSXDC G034.43+00.24 with VERA, and derived its annual parallax of $0.643 \pm 0.049 \text{ mas}$. This corresponds to the distance of $1.56^{+0.12}_{-0.11} \text{ kpc}$, which is less than the half of the previous kinematic distance of 3.7 kpc. We showed that we are able to measure the parallaxes of low-declination source at $\delta_{\text{J2000}} \sim +1^\circ$ with the fitting of right-ascension data only. The stable components of the earth’s atmosphere cause the large scatter in the declination direction of our result.

Since the distance becomes shorter, the masses of millimeter cores decrease by one order of magnitude. The mass of the most massive millimeter core changes from the previous estimations of $\sim 1000M_\odot$ to hundreds M_\odot . The spectral types derived from the luminosity are B1–B3, which are still early B types. The position on Galactic plane is the closer part of Sagittarius-Carina arm. The radial velocity calculated from the flat rotation model has

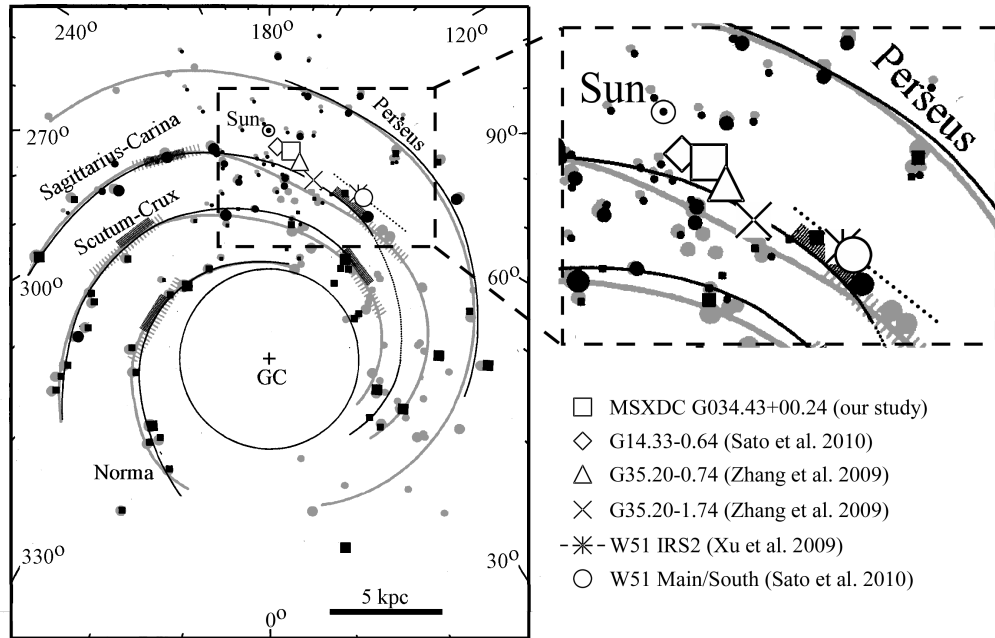


Fig. 10. Positions on the Galactic plane of some sources VLBI parallaxes are measured, overlaid the the model of the Galaxy by Georgelin, Georgelin (1976) (black) and Taylor, Cordes (1993) (gray). “GC” is the position of Galactic center. The open square indicates the position of MSXDC G034.43+00.24 based on our annual parallax measurements. The position of G14.33–0.64 (open diamond) is calculated from the parallax measured by Sato et al. (2010a) from the H₂O maser observations with VERA. The position of G35.20–0.74 (open triangle), G35.20–1.74 (cross) and W51 IRS2 (asterisk) are also based on the parallaxes by Zhang et al. (2009) and Xu et al. (2009) with the VLBA 12-GHz methanol maser observations. The position of W51 Main/South (open circle) is based on the parallax measurements by Sato et al. (2010b) with H₂O maser observations with the VLBA. Uncertainty of distances to W51 IRS2 is shown by the dotted line. The distance uncertainty for the other sources is too small to be hidden by the symbols. [This figure is made from the figure in Sato et al. (2010a).]

a large offset from observed radial velocities by around 40 km s^{-1} , which might be the line-of-sight component of the peculiar motion.

Appendix 1. Details of Data Reduction

Here, we describe the details of our data reduction. Figure 11 shows the procedure of our data reduction and the setting parameters in the AIPS software.

In steps (1) and (2), we read raw data from correlator (FITS files) to AIPS. The AIPS task INDXR (Hereafter, the **CAPITALS OF TYPED FONTS** mean the task or verb (programs) names of AIPS.) was needed for the preparation in the AIPS program. `cparm = 0, 0, 0.02, 0` denotes that the time interval of data calibration is 0.02 minutes. [Hereafter, **small letters of typed fonts** denote the adverbs (setting parameters) of AIPS in the format of

‘(adverb names) = (setting value)’.]

Steps from (3) to (8) were the amplitude calibration for all sources. ACCOR (3) makes the normalizations of visibilities using auto-correlation data. The intervals and integrated durations of this solution were set to 2 minutes with `solint = 2`. After applying this result with CLCAL (4), we carried out the amplitude calibration with the system temperatures and antenna efficiencies. We used system temperatures supplied from Mitaka correlator side. Some antenna efficiencies for different separation angles are supplied from Mitaka correlator, but we used antenna efficiencies at the zero separation angle because there is little change with separation angles¹. We deleted all gain-curve (GC) tables (`inext = GC` and `invers = -1`) with EXTDEST (5) and read new one from the text file of the

¹ VERA Status Report, available from <http://veraserver.mtk.nao.ac.jp/restricted/index-e.html>

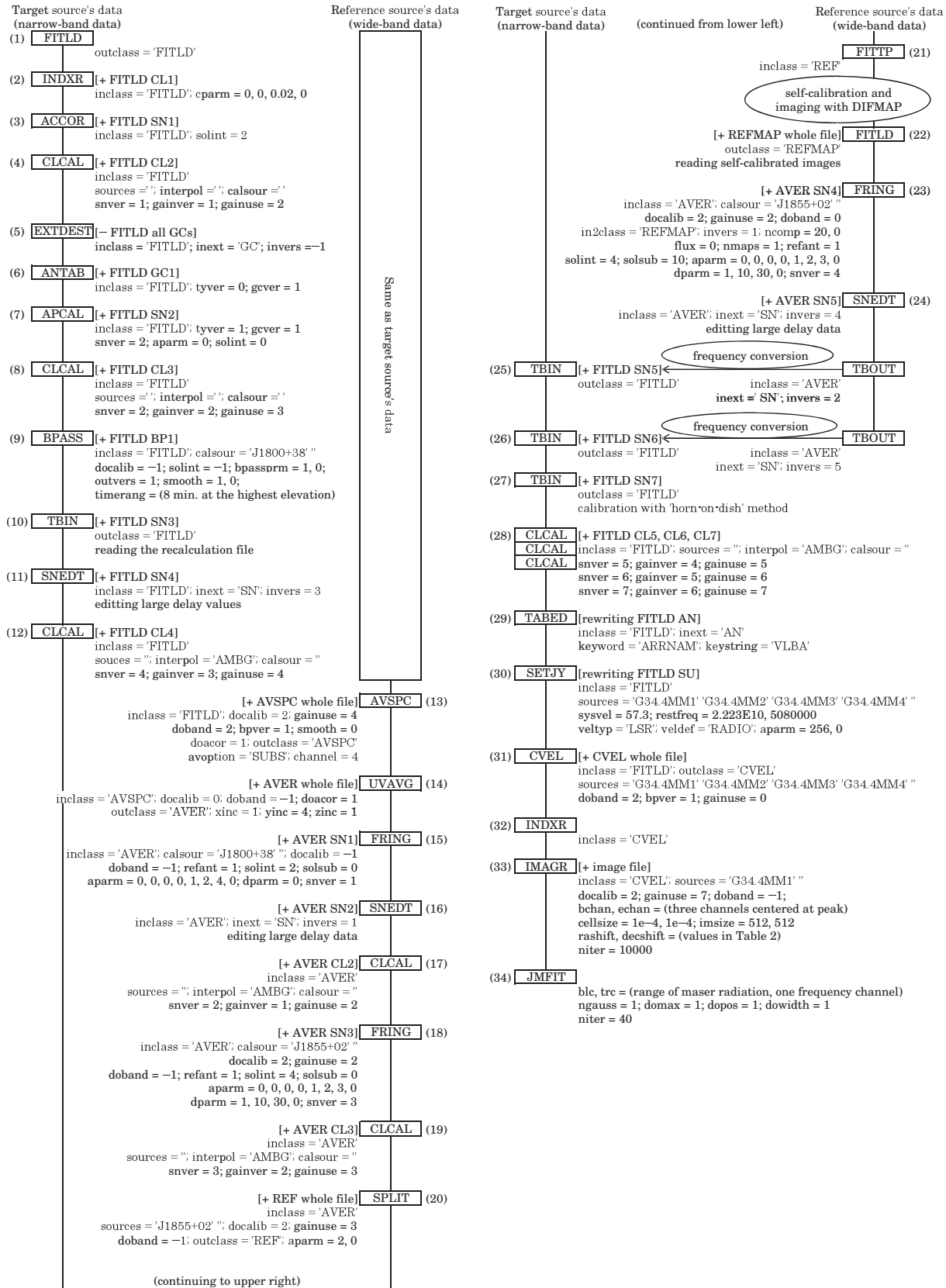


Fig. 11. Details of the data reduction for an observing epoch. Names in the boxes denote AIPS tasks and verbs. Some important adverbs, which are the setting parameters for AIPS tasks and verbs, are shown below the task names in the format of “(adverb name) = (adverb values)”. Square brackets ([...]) show the outputs of the tasks or verbs. Plus signs mean creating new AIPS tables or files. Minus signs mean deleting AIPS tables. AIPS files are denoted with the CLASS names only because NAME parts are used to distinguish observing epochs.

zero separation angle with ANTAB (6). The amplitude calibration itself was done with APCAL (7). This result was also applied with CLCAL (8).

Bandpass calibration was done with BPASS (9). The calibration was applied to all sources by using the data of the calibrator source, QSO J1800+3848 (`calsour = 'J1800+38'`) during 8 minutes at the highest elevation (`solint = -1` and `timerang = (8 min. at the highest elevation)`). We used raw data of the calibrator source without any calibrations (`docalib = -1`). `bpassprm = 1, 0` means that this calibration was done only for the amplitudes, not for the phases. There is little phase variation within and between the IF(s) because VERA uses the digital filter bank for frequency filterings. `smooth = 1, 0` denotes that we apply Hanning smoothing function, whose width is four channels, before bandpass calibration.

Modification of tracking model in Mitaka FX correlator was done by reading a text file with TBIN (10). This text file contains the difference of tracking model between Mitaka FX correlator and CALC3/MSOLV, as explained in §3. We edited large delay data with SNETD (11). This large delays were introduced because of the bug of the program making text files for TBIN. This calibration was applied with CLCAL (12).

Time and frequency integrations were conducted at steps (13) and (14). First frequency integration was carried out with AVSPC. Four frequency channels were integrated to one frequency channel (`avooption = 'SUBS'` and `channel = 4`). This task created new AIPS files, whose visibilities are calibrated with the previous calibrations (`docalib = 2`, `gainuse = 4`, `doband = 2` and `bpver = 1`). `doacor = 1` means that the auto-correlation data are also included in the new AIPS files. Time integration was conducted with UVAVG. Data of 4 ses were integrated to one time step (`xinc = 1`, `yinc = 4` and `zinc = 1`).

Calibration of clock parameters was done with the global fringe search [FRING, (15)] of the calibrator source (`calsour = 'J1800+38'`). The integration time and the time intervals of solutions were 2 minutes (`solint = 2`, `solsub = 0`). The detection threshold was 4 in the signal-to-noise ratio (`aparm = 0, 0, 0, 0, 1, 2, 4, 0`). After editing large delay data with SNETD (16), the results were applied with CLCAL (17), interpolating 2π ambiguity of phases using rate values (`interpol = 'AMBG'`). Then the global fringe search [FRING, (18)] was conducted for the reference source (`calsour = 'J1855+02'`). We set the delay and window of 10 ns and 30 mHz, respectively (`dparm = 1, 10, 30, 0`). This result was also applied with CLCAL (19). After integrating all frequency channels of each IF with SPLIT (20) (`aparm = 2, 0`) and outputting to FITS file with FITTP (21), the reference source was imaged with self-calibration using DIFMAP.

For phase referencing, we reran the global fringe search for the reference source. After loading the image of the reference source with FITLD (22), we carried out the global fringe search with FRING (23). The image is used for the model of the source structure (`ncomp = 20, 0`, `nmaps = 1`). The integration time and the solution intervals

were 4 minutes and 0.4 minutes, respectively (`solint = 4`, `solsub = 10`). Editing large delay data with SNETD (24), this result and the result of calibration of clock parameters were transferred to the target source data (25, 26). Here we needed to convert phases because they depend on frequencies in $\phi = 2\pi\nu\tau$, where ϕ , ν and τ are phase, frequency and delay. After loading the calibration of 'horn-on-dish' method (27), these results were applied (28).

Calibration of Doppler effect in VLBI does not include the earth's spin. AIPS conducts this calibration only when the ARRNAM (array name) keyword in antenna tables is VLBA. So we changed it from VERA to VLBA with task TABED (29). The parameters of Doppler calibration were set with SETJY by rewriting source (SU) tables (30). The frequency channel of $v_{\text{LSR}} = 57.3 \text{ km s}^{-1}$ was moved to the channel number 256 (`sysvel = 57.3`, `veltyp = 'LSR'`, `aparm = 256, 0`). The rest frequency was set to 22.23508 GHz (`restfreq = 2.223E10, 5080000`). The calibration itself was conducted with CVEL (31) for the target sources (`sources = 'G34.4MM1', 'G34.4MM2', 'G34.4MM3', 'G34.4MM4'`). INDXR (32) needed for creating AIPS internal files deleted by CVEL.

Imaging of target source was carried out with IMAGR (33). The imaged source was MM1 (`sources = 'G34.4MM1'`). The size of a pixel was $(1 \times 10^{-4} \text{ mas}) \times (1 \times 10^{-4} \text{ mas})$ (`cellsize 1e-4, 1e-4`). The resultant images had 512×512 pixels (`imsize = 512, 512`). The maximum number of clean components were 10000 (`niter = 10000`). Measurement of positions and fluxes was done by fitting elliptical Gaussians with JMFIT (34). The maximum step of iteration in the fitting was 40 (`niter = 40`).

References

- Asaki, Y., et al. 2007, PASJ, 59, 397
 Baba, J., Asaki, Y., Makino, J., Miyoshi, M., Saitoh, T. R., & Wada, K. 2009, ApJ, 706, 471
 Bronfman, L., Nyman, L.-Å., & May, J. 1996, A&AS, 115, 81
 Carey, S. J., Clark, F. O., Egan, M. P., Price, S. D., Shipman, R. F., & Kuchar, T. A. 1998, ApJ, 508, 721
 Carey, S. J., Feldman, P. A., Redman, R. O., Egan, M. P., MacLeod, J. M., & Price, S. D. 2000, ApJ, 543, L157
 Chambers, E. T., Jackson, J. M., Rathborne, J. M., & Simon, R. 2009, ApJS, 181, 360
 Charlot, P. 1990, AJ, 99, 1309
 Downes, D., Wilson, T. L., Bieging, J. & Wink, J. 1980, A&AS, 40, 379
 Egan, M. P., Shipman, R. F., Price, S. D., Carey, S. J., Clark, F. O., & Cohen, M. 1998, ApJ, 494, L199
 Faúndez, S., Bronfman, L., Garay, G., Chini, R., Nyman, L.-Å., & May, J. 2004, A&A, 426, 97
 Fomalont, E. B., Petrov, L., MacMillan, D. S., Gordon, D. & Ma, C. 2003, AJ, 126, 2562
 Fujishita, M. 1983, Publ. Int. Latitude Obs. Mizusawa, 17, 13
 Georgelin, Y. M. & Georgelin, Y. P. 1976, A&A, 49, 57
 Garay, G., Faúndez, S., Mardones, D., Bronfman, L., Chini, R., & Nyman, L.-Å. 2004, ApJ, 610, 313
 Green, R. M. 1985, Spherical Astronomy (Cambridge : Cambridge University Press)

- Hennebelle, P., Pérault, M., Teyssier, D., & Ganesh, S. 2001, *A&A*, 365, 598
- Honma, M., et al. 2008, *PASJ*, 60, 935
- Honma, M., Tamura, Y., & Reid, M. J. 2008, *PASJ*, 60, 951
- Iguchi, S., Kurayama, T., Kawaguchi, N., & Kawakami, K. 2005, *PASJ*, 57, 259
- Jackson, J. M., Finn, S. C., Rathborne, J. M., Chambers, E. T., & Simon, R. 2008, *ApJ*, 680, 349
- Jike, T., Fukuzaki, Y., Shibuya, K., Doi, K., Manabe, S., Jauncey, D. L., Nicolson, G. D., & McCulloch, P. M. 2005, *Polar Geosci.*, 18, 26
- Kamohara, R., et al. 2010, *A&A*, 510, A69
- Kawaguchi, N., Sasao, T., & Manabe, S. 2000, *Proc. SPIE*, 4015, 544
- Kurayama, T., Sasao, T., & Kobayashi, H. 2005, *ApJ*, 627, L49
- Manabe, S., Yokoyama, K., & Sakai, S. 1991, *IERS Techn. Note*, 8, 61
- Miralles, M. P., Rodríguez, L. F., & Scalise, E. 1994, *ApJS*, 92, 173
- Molinari, S., Brand, J., Cesaroni, R., Palla, F., & Palumbo, G. G. C. 1998, *A&A*, 336, 339
- Motogi, K., Sorai, K., Habe, A., Honma, M., Kobayashi, H., & Sato, K. 2011, *PASJ*, 63, 31
- Oh, C. S., Kobayashi, H., Honma, M., Hirota, T., Sato, K., & Ueno, Y. 2010, *PASJ*, 62, 101
- Pérault, M., et al. 1996, *A&A*, 315, L165
- Pillai, T., Wyrowski, F., Carey, S. J., & Menten, K. M. 2006, *A&A*, 450, 569
- Rathborne, J. M., Jackson, J. M., Chambers, E. T., Simon, R., Shipman, R., & Frieswijk, W. 2005, *ApJ*, 630, L181
- Rathborne, J. M., Jackson, J. M., & Simon, R. 2006, *ApJ*, 641, 389
- Rathborne, J. M., Simon, R., & Jackson, J. M. 2007, *ApJ*, 662, 1082
- Rygl, K. L. J., Brunthaler, A., Reid, M. J., Menten, K. M., van Langevelde, H. J., & Xu, Y. 2010, *A&A*, 511, A2
- Sato, M., Hirota, T., Reid, M. J., Honma, M., Kobayashi, H., Iwadate, K., Miyaji, T., & Shibata, K. M. 2010a, *PASJ*, 62, 287
- Sato, M., Reid, M. J., Brunthaler, A., & Menten, K. M. 2010b, *ApJ*, 720, 1055
- Sanhueza, P., Garay, G., Bronfman, L., Mardones, D., May, J., & Saito, M. 2010, *ApJ*, 715, 18
- Shepherd, D. S., et al. 2007, *ApJ*, 669, 464
- Simon, R., Jackson, J. M., Rathborne, J. M., & Chambers, E. T. 2006a, *ApJ*, 639, 227
- Simon, R., Rathborne, J. M., Shah, R. Y., Jackson, J. M., & Chambers, E. T. 2006b, *ApJ*, 653, 1325
- Taylor, J. H. & Cordes, J. M. 1993, *ApJ*, 411, 674
- Tayssier, D., Hennebelle, P., & Pérault, M. 2002, *A&A*, 382, 624
- Thompson, A. R., Moran, J. M., & Swenson, G. W., Jr. 2001, *Interferometry and Synthesis in Radio Astronomy*, 2nd edition (New York: John Wiley & Sons)
- Wang, Y., Zhang, Q., Rathborne, J. M., Jackson, J., & Wu, Y. 2006, *ApJ*, 651, L125
- Xu, Y., Reid, M. J., Menten, K. M., Brunthaler, A., Zheng, X. W. & Moscadelli, L. 2009, *ApJ*, 693, 413
- Zhang, B., Zheng, X. W., Reid, M. J., Menten, K. M., Xu, Y., Moscadelli, L. & Brunthaler, A. 2009, *ApJ*, 693, 419